




## Absence of backscattering in Fermi-arc mediated conductivity of the topological Dirac semimetal $\text{Cd}_3\text{As}_2$

Vsevolod Ivanov <sup>1,2,3</sup>, Lotte Borkowski <sup>4</sup>, Xiangang Wan,<sup>5</sup> and Sergey Y. Savrasov <sup>4,5</sup>

<sup>1</sup>Virginia Tech National Security Institute, Blacksburg, Virginia 24060, USA

<sup>2</sup>Department of Physics, Virginia Tech, Blacksburg, Virginia 24061, USA

<sup>3</sup>Virginia Tech Center for Quantum Information Science and Engineering, Blacksburg, Virginia 24061, USA

<sup>4</sup>Department of Physics, University of California, Davis, California 95616, USA

<sup>5</sup>National Laboratory of Solid State Microstructures, School of Physics and Collaborative Innovation Center of Advanced Microstructures, Nanjing University, Nanjing 210093, China



(Received 29 January 2024; revised 19 March 2024; accepted 24 April 2024; published 10 May 2024)

Having previously been the subject of decades of semiconductor research, cadmium arsenide ( $\text{Cd}_3\text{As}_2$ ) has now reemerged as a topological material, realizing ideal three-dimensional Dirac points at the Fermi level. These topological Dirac points lead to a number of extraordinary transport phenomena, including strong quantum oscillations, large magnetoresistance, ultrahigh mobilities, and Fermi velocities exceeding graphene. The large mobilities persist even in thin films and nanowires of  $\text{Cd}_3\text{As}_2$ , suggesting the involvement of topological surface states. However, computational studies of the surface states in this material are lacking, in part due to the large 80-atom unit cell. Here we present the computed Fermi-arc surface states of a  $\text{Cd}_3\text{As}_2$  thin film, based on a tight-binding model derived directly from the electronic structure. We show that despite the close proximity of the Dirac points, the Fermi arcs are very long and straight, extending through nearly the entire Brillouin zone. The shape and spin properties of the Fermi arcs suppress both back- and side scattering at the surface, which we show by explicit integrals over the phase space. The introduction of a small symmetry-breaking term, expected in a strong electric field, gaps the electronic structure, creating a weak topological insulator phase that exhibits similar transport properties. Crucially, the mechanisms suppressing scattering in this material differ from those in other topological materials such as Weyl semimetals and topological insulators, suggesting a new route for engineering high-mobility devices based on Dirac semimetal surface states.

DOI: [10.1103/PhysRevB.109.195139](https://doi.org/10.1103/PhysRevB.109.195139)

### I. INTRODUCTION

Cadmium arsenide ( $\text{Cd}_3\text{As}_2$ ) is a well-known semiconductor that has been thoroughly studied for the greater part of a century for its remarkable transport properties [1]. More recently, this material was predicted [2] and confirmed using angle-resolved photoemission spectroscopy [3–6] to be a topological Dirac semimetal. A conventional Dirac semimetal exists at the boundary between topological insulator (TI) and normal insulator phases in a system possessing both time-reversal and inversion symmetries, and hosts a Dirac node at a time-reversal invariant momentum point in the Brillouin zone (BZ) [7]. However, such a phase can also exist when the crystal structure possesses a rotational axis [8], such as the  $C_4$  rotation in  $\text{Cd}_3\text{As}_2$ , which can result in accidental band crossings at the Fermi energy, leading to two topologically protected Dirac points along the  $\Gamma$ -Z direction [2].

The properties of  $\text{Cd}_3\text{As}_2$  have been well established through a number of experimental works, in which it served as a prototypical system for demonstrating the optical conductivity [9–11], quantum oscillations [12–14], and electronic transport [15–21] of Dirac semimetal materials. Dirac semimetals were additionally predicted to exhibit proximity-induced superconductivity [22], and  $\text{Cd}_3\text{As}_2$  was used in experimental realizations of this effect [23–26].

Cadmium arsenide also received limited theoretical treatment using models [2,27] and first-principles calculations [2,28–31], which are inherently limited by the large number of atoms (80) in its primitive unit cell. In particular, this makes first-principles investigations of the surface state physics of  $\text{Cd}_3\text{As}_2$  especially difficult on account of the even larger supercells involved.

The Dirac points in  $\text{Cd}_3\text{As}_2$  can be considered as composed of opposite chirality Weyl points, which are connected by Fermi arcs at the material surface [32]. It has been shown that the Fermi arcs in Weyl semimetals can be highly conductive [33], prompting the question of whether the Fermi-arc states of Dirac semimetals can lead to similar transport effects. This question is particularly relevant for the case of  $\text{Cd}_3\text{As}_2$ , which has been shown to exhibit extraordinarily high electronic transport even in thin-film and nanowire geometries [12,16,19,34,35], where surface effects would be expected to dominate.

Here we perform a numerical study of the electronic transport of  $\text{Cd}_3\text{As}_2$  mediated by its Fermi-arc surface states. We begin by empirically deriving a tight-binding model fit to the first-principles electronic structure, and use it to construct a 40-layer slab supercell to extract the surface energy bands. We show that in contrast to prior  $\mathbf{k} \cdot \mathbf{p}$  models [2], the Fermi arcs of  $\text{Cd}_3\text{As}_2$  in our *ab initio*-based model are long and straight,

extending across the entire BZ to connect across the zone boundary. By performing explicit calculations of the phase space available to electronic scattering we demonstrate that two major scattering contributions become vanishingly small regardless of the scattering mechanism. This can potentially lead to very high conductance in thin films of  $\text{Cd}_3\text{As}_2$ . We further extend this argument in the presence of an external electric field, where we show that the induced symmetry breaking results in a weak topological insulator phase, whose surface states preserve the essential properties necessary for high electronic mobility. We conclude by discussing how these results might lead to next-generation electronic devices based on the high electronic mobility of the surface states and their potential hydrodynamic transport, and how such long, straight Fermi arcs might be engineered in semiconductor heterostructures.

## II. MATERIAL BACKGROUND

Although research on the properties of  $\text{Cd}_3\text{As}_2$  has been reinvigorated by the confirmation of its topological electronic structure [3], the material itself has been known to exist for nearly a century [1]. At high temperatures,  $\text{Cd}_3\text{As}_2$  adopts an antiferroite structure ( $Fm\bar{3}m$ , No. 225) with two cadmium vacancies [1]. Upon cooling to  $\sim 600^\circ\text{C}$ , the remaining cadmium atoms displace towards the ordered vacancies, resulting in an intermediate structure ( $P4_2/nmc$ , No. 137) of the original cubic structure [36]. Below  $\sim 475^\circ\text{C}$ , the material settles into its low-temperature phase, which is a superstructure with a tetragonal unit cell with  $a = 12.63 \text{ \AA}$  and  $c = 25.427 \text{ \AA}$  [31]. The exact nature of this low-temperature phase has been somewhat controversial, initially being assigned to the inversion-broken  $I4_1cd$  (No. 110) space group [37], which was recently reexamined and found to actually be the centrosymmetric  $I4_1acd$  (No. 142) [31]. This has important consequences for the electronic structure, preserving the Dirac crossings in the BZ, and enabling the possibility of tuning the topological phase by breaking inversion symmetry.

The topological nature of the electronic structure in  $\text{Cd}_3\text{As}_2$  has been confirmed experimentally with transport and angle-resolved photoemission spectroscopy (ARPES) measurements.

Electronic excitations around the Dirac cones at the Fermi level of  $\text{Cd}_3\text{As}_2$  behave like relativistic Dirac fermions with linear dispersion. These excitations have extremely large Fermi velocities [16] and are expected to lead to large electronic mobilities, which have been observed experimentally [16,18,19]. Surprisingly, these high electron mobilities persist even in thin films and nanowires of  $\text{Cd}_3\text{As}_2$  [16,27,34,35]. Bulk-boundary correspondence in topological materials [38] implies that topological features in the bulk exist in tandem with topologically protected surface states, which in the case of bulk Dirac points take the form of Fermi arcs connecting their projections on the surface. Such Fermi arcs are known to be highly conductive for related Weyl semimetal systems [33] and would be expected to dominate the transport properties of  $\text{Cd}_3\text{As}_2$  in thin-film and nanowire geometries.

ARPES measurements enable the direct observation of bulk and surface states. This has allowed the linearly dispersing Dirac cones at the Fermi surface to be directly observed

[3–6]. The derived  $\mathbf{k} \cdot \mathbf{p}$  model [2] predicts the existence of short Fermi arcs enclosing the  $\Gamma$  point, and later studies of the Weyl-semimetal state in symmetry-broken  $\text{Cd}_3\text{As}_2$  using a model derived from Wannier interpolation also predict short arcs [30]. However, the  $\mathbf{k} \cdot \mathbf{p}$  model necessarily represents only the behavior near the  $\Gamma$  point, poorly capturing the electronic structure at the BZ edge, and experimental ARPES measurements have yet to observe Fermi-arc surface states. It has been suggested that the difficulty in observing Fermi-arc surface states in Dirac semimetals might stem from their lack of topological protection [39], and in fact there exist Dirac systems that completely lack Fermi arcs [40].

Directly simulating these surface states from first principles would be computationally prohibitive, as such a calculation would require a slab supercell consisting of at least several dozen enormous unit cells of  $\text{Cd}_3\text{As}_2$ . The inclusion of spin-orbit coupling in order to correctly capture the topological electronic structure and the dense  $\mathbf{k}$ -point grids needed to obtain the Fermi surface would further complicate this approach. On the other hand, a  $\mathbf{k} \cdot \mathbf{p}$  model, while quick to compute, would not be able accurately represent the electronic structure throughout the entire BZ. The most optimal approach, which admits a trade-off of speed and accuracy, is a tight-binding model.

## III. ELECTRONIC STRUCTURE OF $\text{Cd}_3\text{As}_2$

We perform self-consistent density functional-based electronic structure calculation of  $\text{Cd}_3\text{As}_2$  using the full potential linear muffin-tin orbital method (FP-LMTO) including spin-orbit coupling [41]. The LMTO basis contains  $s$ ,  $p$ , and  $d$  orbitals for Cd and for As with two different tail energies taken at 0 and  $-13.6 \text{ eV}$ . The nonspherical terms of the potential and the density are expanded in spherical harmonics till  $l_{\text{max}} \leq 6$  inside the muffin-tin spheres and are represented by  $80 \times 80 \times 100$  fast Fourier transform grid in the interstitial region. The local density approximation of Ref. [42] is utilized.

We plot the band structure along the  $Z$ - $\Gamma$ - $X$  direction in Fig. 1. It clearly reveals the fourfold degenerate Dirac point along the  $\Gamma$ - $Z$  direction, which is protected by the  $C_4$  rotational symmetry of the crystal [8] and is consistent with previous studies of  $\text{Cd}_3\text{As}_2$  [31]. The low-energy states are primarily composed from the Cd  $-5s$  and As  $-4p$  orbitals as has been discussed in Ref. [2], and the nature of the band inversion in this system can be understood in terms of the 4-orbitals involving Cd  $-5s$   $\Gamma_6$  and As  $-4p$   $\Gamma_7$  relativistic states [2].

In order to numerically study the topological surface states of  $\text{Cd}_3\text{As}_2$  and their transport properties, a low-energy model in the vicinity of the Fermi level is needed. Here we are primarily interested in capturing a spin texture of the states crossing the Fermi level, since the discovery of topological insulators and the associated Weyl and Dirac semimetals specifically emphasized the connection between the spin and the momentum of the topological states, which has been at the heart of our understanding properties of such systems [43,44]. This has been related to the spin momentum locking of the surface Dirac cones seen in a vast majority of topological insulators, as well as the all-in (all-out) structure of spins around

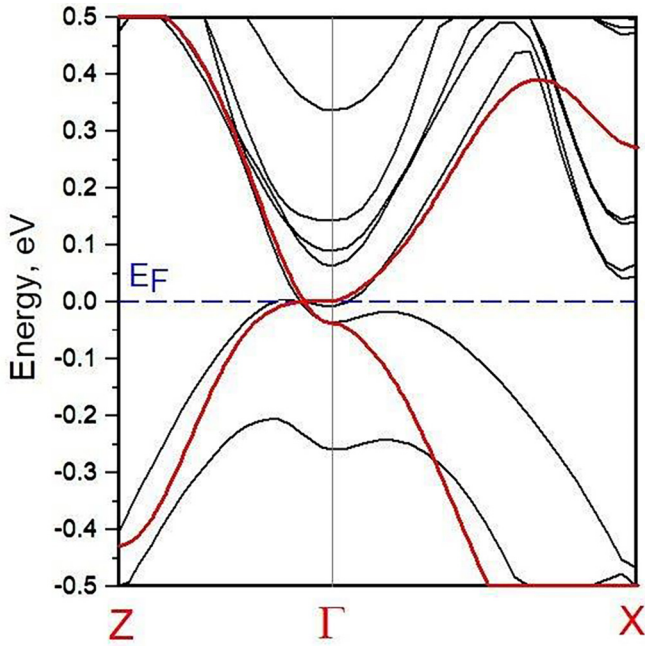


FIG. 1. Electronic structure of  $\text{Cd}_3\text{As}_2$  derived from first-principles density functional-based calculation (black) and its tight-binding fit (red).

the Weyl points in Weyl and Dirac semimetals leading to the notion of negative (positive) chiral charges. It has also been shown that the spin momentum-locking feature persists for the Fermi-arc surface states, for which orbital effects, although they exist, are not really significant, and the surface transport phenomena are frequently discussed under the assumption of the spin as a good quantum number.

Therefore, we derive a minimal two-band tight-binding model by empirically fitting the electronic structure. Our model captures the essence of the electronic behavior throughout the BZ and accurately reproduces the fourfold topological Dirac point along the  $\Gamma$ -Z direction as shown in red in Fig. 1. (We describe the tight-binding fit and list the parameters of the model in Appendix A.)

Using this tight-binding model we construct a 40-layer slab in the  $\langle 110 \rangle$  direction, by first extending the model over the supercell and then forbidding hoppings between the top and bottom surfaces. The relationship between BZs for the bulk and the slab is shown in Fig. 2.

The resulting band structure can be plotted within the plane spanned by the  $k_{(1-10)} = k_{xy}$  and  $k_{(001)} = k_z$  vectors, shown in Fig. 3(a). The surface states arising from the topological Dirac nodes are clearly visible as the only states crossing the Fermi energy.

Plotting the Fermi surface of the slab calculation reveals that the two Dirac point projections are connected by very long, straight Fermi arcs [Fig. 3(b)]. In contrast to the  $\mathbf{k} \cdot \mathbf{p}$  calculations [2], these arcs do not enclose the  $\Gamma$  point, and instead extend through the entire BZ to connect across the BZ boundary. The main difference between our and previous calculations can be understood from the range of the hopping integrals: the  $\mathbf{k} \cdot \mathbf{p}$  theory assumes periodization, that is, when one replaces  $k$  by  $\sin(k)$  and  $k^2$  by  $1 - \cos(k)$ , which would

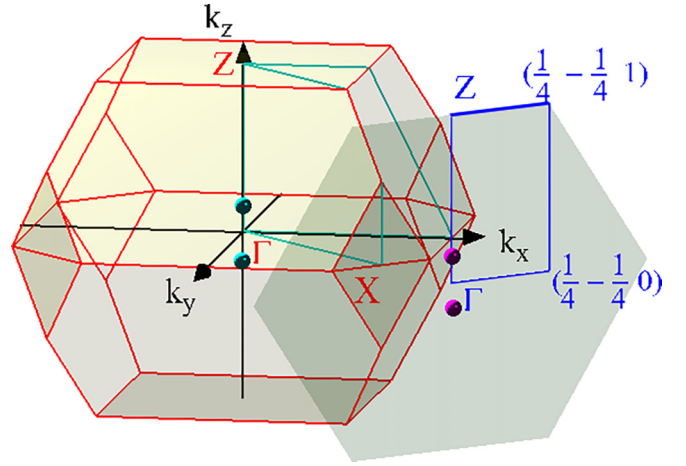


FIG. 2. Brillouin zone (BZ) of bulk  $\text{Cd}_3\text{As}_2$  and its projection along the  $\langle 110 \rangle$  direction that is used for calculating the surface states. The blue rectangle shows the portion of the surface BZ that will be used in subsequent plots. The bulk Dirac points along  $\Gamma$ -Z and their projections onto the surface BZ are indicated by small circles.

include nearest-neighbor hopping integrals only, while a good description of the Fermi states in  $\text{Cd}_3\text{As}_2$  requires rather long-range hoppings up to the fourth nearest neighbor, as we elaborate in Appendix A.

The origin of the arcs is revealed in terms of the  $\pm$  chirality Weyl points making up each Dirac point. Each pair of Weyl points located at opposite momentum space  $k$  points are connected by a single Fermi arc. The two Dirac points of  $\text{Cd}_3\text{As}_2$  can be thought of as two pairs of coincident Weyl points of antialigned chiralities, with each pair having its own Fermi arc. An important feature of the Fermi arcs is the spin texture: spins along each arc point along opposite directions, but rotating as they approach the Dirac node projections to align with a local “all-out” arrangement around each point.

#### IV. TRANSPORT ANALYSIS

We now proceed to the analysis of the surface-mediated transport in  $\text{Cd}_3\text{As}_2$  from first principles. The relaxation rate of the electrons due to impurities or phonons is related to the matrix element of their scattering potential. This usually results in a temperature-independent impurity contribution to the resistivity of a metal often seen at very low temperatures, with an electron-phonon contribution that scales linearly with temperature,  $\rho_{e-ph}(T) \propto \lambda_{tr} T$ , where  $\lambda_{tr}$  is the so-called transport coupling constant, which captures the scattering processes of the electrons near the Fermi surface. It can be obtained from an integral over the BZ  $\lambda_{tr} = \sum_{\mathbf{q}} \lambda_{tr}(\mathbf{q})$  [45], of various scattering events subjected to the momentum and energy conservation laws:

$$\lambda_{tr}(\mathbf{q}) \sim \sum_{\mathbf{k}} (v_{\mathbf{k}\alpha} - v_{\mathbf{k}+\mathbf{q}\alpha})^2 |V_{\mathbf{k}\mathbf{k}+\mathbf{q}}|^2 \delta(\epsilon_{\mathbf{k}}) \delta(\epsilon_{\mathbf{k}+\mathbf{q}}). \quad (1)$$

Here  $\epsilon_{\mathbf{k}}$ ,  $\epsilon_{\mathbf{k}+\mathbf{q}}$  are the energies and  $v_{\mathbf{k}\alpha}$ ,  $v_{\mathbf{k}+\mathbf{q}\alpha}$  are the Fermi velocities at points  $\mathbf{k}$ ,  $\mathbf{k} + \mathbf{q}$  in the phase space. The delta functions  $\delta(\epsilon_{\mathbf{k}})$ ,  $\delta(\epsilon_{\mathbf{k}+\mathbf{q}})$  constrain scattering to the Fermi surface. The transport direction is set by  $\alpha = x, y, z$ , while  $V_{\mathbf{k}\mathbf{k}+\mathbf{q}}$  is the matrix element taken over the spinor wave functions

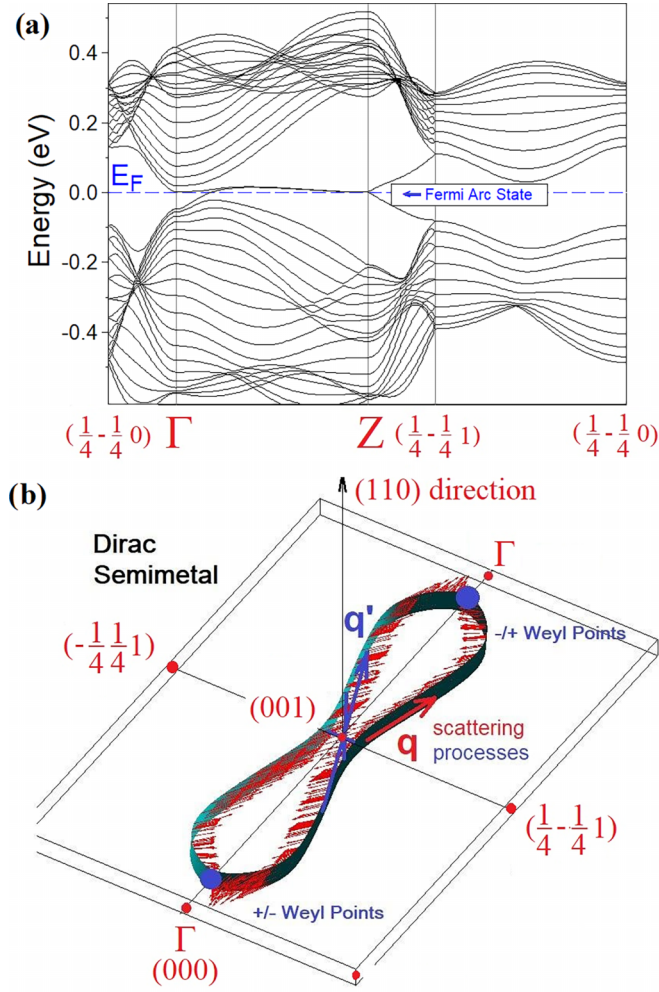


FIG. 3. Forty-layer slab calculation of the tight-binding model fit for the Dirac semimetal phase of  $\text{Cd}_3\text{As}_2$ , showing the (a) band structure and (b) Fermi-arc surface states. Note that the shown region is stretched along the  $k_{\langle 110 \rangle}$  direction in order to more clearly show the arc shape.

$\vec{\psi}_{\mathbf{k}}(\mathbf{r})$  of the electrons with a potential  $V(\mathbf{r})$  arising from either impurities or atomic displacements induced by a phonon with wave vector  $\mathbf{q}$ :

$$= \langle \vec{\psi}_{\mathbf{k}} | V | \vec{\psi}_{\mathbf{k}+\mathbf{q}} \rangle. \quad (2)$$

Generally, electron-phonon resistivity calculations can be carried out for real materials from completely first principles [33,46]. The same is true for supercell simulations with impurities; however, the large unit cell of  $\text{Cd}_3\text{As}_2$  expanded to a 40-layer slab contains thousands of atoms and would make such direct approaches computationally intractable. Instead we use the assumption that is in the heart of the physics of topological materials, namely, that the spin is approximately a good quantum number. This allows us to represent the spinor wave function  $\vec{\psi}_{\mathbf{k}}$  entering the matrix element, Eq. (2), with spin and spatial degrees of freedom in a separable form:

$$\vec{\psi}_{\mathbf{k}}(\mathbf{r}) = \begin{pmatrix} \chi^{(1)}(\mathbf{k}) \\ \chi^{(2)}(\mathbf{k}) \end{pmatrix} \phi_{\mathbf{k}}(\mathbf{r}) = \vec{\chi}(\mathbf{k}) \phi_{\mathbf{k}}(\mathbf{r}). \quad (3)$$

The spin part  $\vec{\chi}(\mathbf{k})$  is given by

$$\vec{\chi}_{\mathbf{k}} = \begin{pmatrix} e^{-i\varphi_{\mathbf{k}}/2} \cos(\theta_{\mathbf{k}}/2) \\ e^{+i\varphi_{\mathbf{k}}/2} \sin(\theta_{\mathbf{k}}/2) \end{pmatrix}. \quad (4)$$

Here the angles  $\varphi_{\mathbf{k}}$ , and  $\theta_{\mathbf{k}}$  describe the direction of the spin at  $\mathbf{k}$  in spherical coordinates and can be easily evaluated during the course of the electronic structure calculation. As a result, the matrix element  $V_{\mathbf{k}\mathbf{k}+\mathbf{q}}$  for nonmagnetic scatterers has a factored form

$$V_{\mathbf{k}\mathbf{k}+\mathbf{q}} = \langle \vec{\chi}_{\mathbf{k}} | \vec{\chi}_{\mathbf{k}+\mathbf{q}} \rangle \langle \phi_{\mathbf{k}} | V | \phi_{\mathbf{k}+\mathbf{q}} \rangle, \quad (5)$$

where the spinor part

$$\langle \vec{\chi}_{\mathbf{k}} | \vec{\chi}_{\mathbf{k}+\mathbf{q}} \rangle \equiv V_{\mathbf{k}\mathbf{k}+\mathbf{q}}^{\text{spin}} \quad (6)$$

can be taken into account in the transport analysis without a detailed knowledge of the scattering potential  $V(\mathbf{r})$ .

Thus, we use our previously derived tight-binding fit to perform the analysis of the phase space available to the scattering using Eq. (1) with only the spinor contribution to the matrix element,  $V_{\mathbf{k}\mathbf{k}+\mathbf{q}}^{\text{spin}}$ , and derive our conclusions based on this phase space calculation. For a slab extended in the  $\langle 110 \rangle$  direction, the BZ will be highly compressed along  $k_{\langle 110 \rangle}$ , therefore we use a two-dimensional  $800 \times 800$   $\mathbf{k}$ -point grid for the integration in Eq. (1). Since the Fermi arcs are very narrow along the  $k_{\langle 110 \rangle}$  direction, the  $\mathbf{q}$ -point region for visualizing  $\lambda_{rr}(\mathbf{q})$  is selected to be a part of the BZ, spanned by the corners  $(1/4, -1/4, 0)$ ,  $(-1/4, 1/4, 0)$  in the  $(2\pi/a, 2\pi/a, 2\pi/c)$  units of the reciprocal space.

Before discussing the numerical results, we qualitatively consider the behavior of the phase space available to scattering. We will be assuming a thin-film setup of  $\text{Cd}_3\text{As}_2$  so that the number of bulk carriers is relatively small and the arc to bulk scattering can be neglected. This is essential, since in the thermodynamic limit for the bulk, a spatially homogeneous field will always produce a nonzero bulk current due to thermal excitations, disorder, and electronic correlations even in ideal scenarios with the Fermi level pinned at the Dirac points, and this will overwhelm all surface effects. The main contributions to  $\lambda_{rr}(\mathbf{q})$  are known to be the backscattering processes, since in this case the electronic velocities entering Eq. (1) will be oppositely directed. The backscattering ( $\mathbf{k} \rightarrow -\mathbf{k}$ ) occurs in every three-dimensional Fermi surface but would be absent for a true Weyl semimetal since its Fermi arcs reside on the different surfaces. However, this is no longer true in a Dirac semimetal where both Fermi arcs appear at the same surface. We, however, notice that aside from small regions near the Dirac point projections, the spinor states on opposite Fermi arcs are antialigned, as seen in Fig. 3(b). This makes such backscattering processes strongly cancel each other for nonmagnetic impurities or phonons due to the orthogonality of spinors with opposite spins. To see this explicitly, we notice that the spins of the surface electrons align entirely within the surface [Fig. 3(b)]. This allows us to set  $\varphi_{\mathbf{k}} = 0$  in Eq. (4), and  $V_{\mathbf{k}\mathbf{k}+\mathbf{q}}^{\text{spin}}$  is simplified to

$$V_{\mathbf{k}\mathbf{k}+\mathbf{q}}^{\text{spin}} = \sqrt{\frac{1}{2}[1 + \cos(\theta_{\mathbf{k}} - \theta_{\mathbf{k}+\mathbf{q}})]}.$$

For the backscattering events,  $\theta_{\mathbf{k}+\mathbf{q}} = \theta_{\mathbf{k}} + \pi$ ,  $V_{\mathbf{k}\mathbf{k}+\mathbf{q}}^{\text{spin}}$  vanishes.

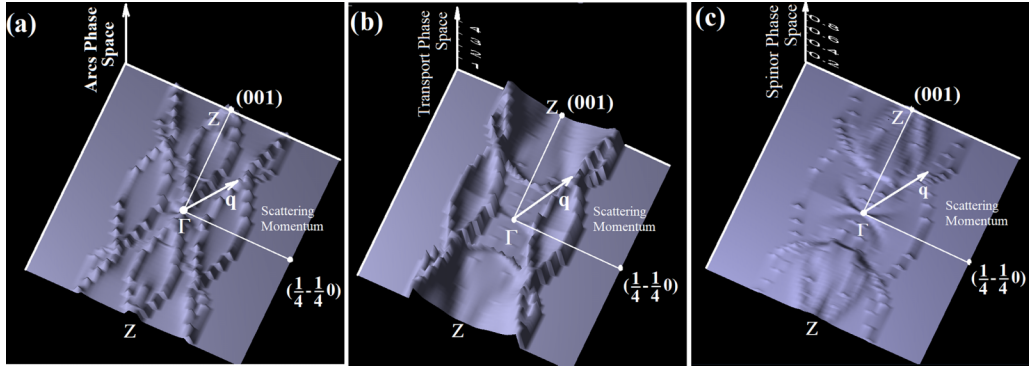


FIG. 4. Phase space calculation of scattering processes involving Fermi-arc electrons in  $\text{Cd}_3\text{As}_2$ . Case (a) is the double-delta integral, (b) includes the velocity prefactor, and (c) includes both velocity and spin prefactors. Note that the normalization factor in (a) differs from the other two plots so only (b) and (c) can be compared quantitatively.

In contrast, side scattering ( $\mathbf{k} \rightarrow \mathbf{k}'$ ) can occur between any two momentum points along each Fermi arc. The magnitude of this contribution depends on the Fermi velocity term  $(v_{\mathbf{k}\alpha} - v_{\mathbf{k}+\mathbf{q}\alpha})^2$ , where the velocities are oriented perpendicularly to the arc. For the long, straight, Fermi arcs that we find in  $\text{Cd}_3\text{As}_2$ , electrons are only scattered between states with parallel velocities, thus reducing this contribution to zero, much like the case for Fermi-arc states in a Weyl semimetal such as TaAs [33] and NbAs [47].

These contributions can be visualized (Fig. 4) in the  $\mathbf{q}$  dependence of the phase space integral by adding each term in the expression (1) iteratively. First, we evaluate the bare contribution  $\sum_{\mathbf{k}} \delta(\epsilon_{\mathbf{k}}) \delta(\epsilon_{\mathbf{k}+\mathbf{q}})$ , shown in Fig. 4(a). The effect of the dumbbell-like structure of the Fermi arcs is apparent here, forming two bright bands flanking a central bowtie shape along the central strip of the  $\mathbf{q}$  space. While this term lacks the velocity prefactor of the full expression and cannot be quantitatively compared to the other calculations, it clearly shows all of the allowed transitions within the phase space.

Next we add the velocity contribution, computing the integral  $\sum_{\mathbf{k}} (v_{\mathbf{k}\alpha} - v_{\mathbf{k}+\mathbf{q}\alpha})^2 |\delta(\epsilon_{\mathbf{k}}) \delta(\epsilon_{\mathbf{k}+\mathbf{q}})|$ , shown in Fig. 4(b). This greatly reduces the amplitude of side-scattering processes along the Fermi arcs extended in the  $q_z$  direction, evidenced by the disappearance of the central bowtie structure in the phase space.

We can also quantitatively compare the effect of including the spinor term  $\sum_{\mathbf{k}} (v_{\mathbf{k}\alpha} - v_{\mathbf{k}+\mathbf{q}\alpha})^2 |V_{\mathbf{k}\mathbf{k}+\mathbf{q}}^{\text{spin}}|^2 \delta(\epsilon_{\mathbf{k}}) \delta(\epsilon_{\mathbf{k}+\mathbf{q}})$ , since for nonmagnetic scatterers this results in evaluating the overlap between two spinor states of the electrons. The result is shown in Fig. 4(c), where we also indicate the scales of the obtained phase space functions since the integrals with and without  $|V_{\mathbf{k}\mathbf{k}+\mathbf{q}}^{\text{spin}}|^2$  have the same units. As one sees, the effect of including the spinor overlaps results in complete suppression of the backscattering terms, making contributions to  $\lambda_{rr}$  almost negligible throughout the entire phase space, as evidenced in Fig. 4(c) and its comparison with Fig. 4(b) (notice difference in scales). The only remaining contributions are faint regions at the edge, which correspond to weak scattering terms between  $\mathbf{k}$  points located near opposite Dirac node projections.

The results obtained here can naturally explain recent low temperature measurements of the resistivity of  $\text{Cd}_3\text{As}_2$  [18],

where it was found that some samples below 5 K exhibit very long transport life times which are  $10^4$  longer than the quantum life times. The resistivity anisotropy was seen to be 20–30 in samples with large lifetime enhancements, and ultra-high carrier mobilities have been measured that were claimed to be protected by an “unknown mechanism” [18]. Although such a behavior would indeed be unexpected for bulk Dirac cone states in  $\text{Cd}_3\text{As}_2$ , it is easily understood if the surface transport at very low temperatures is taken into account. At temperatures below 5 K, we expect that thermally activated carriers in the bulk Dirac band would essentially be absent.

It has been a remarkable property of the topological surface states to be resilient to the defects at the surface, therefore we do not anticipate that a small surface disorder will have a big impact on the shape and spin texture of the topological Fermi arcs. Thus, the Fermi-arc surface states should be contributing to the conductivity in a realistic device setup, where strong anisotropy and very large carrier mobility are expected to occur as seen from our phase space calculation. There is, however, a possibility that the bulk Dirac points are slightly gapped due to some structural distortions that can naturally occur during crystal growth or in the vicinity of the contact with leads. We discuss the results of our calculations with the structural distortions in the following section.

## V. TOPOLOGICAL INSULATOR PHASE

Here we analyze the electronic structure of  $\text{Cd}_3\text{As}_2$  in the presence of structural distortions that can occur either by applying a strong electric field along the  $\langle 110 \rangle$  growth direction or due to the presence of the electrical contact. Such perturbation will necessarily break the inversion and  $C_4$  rotation symmetries of the system, and would expectantly introduce a small gap at the Dirac points. This symmetry-breaking effect can be modeled at the level of the crystal structure by introducing small opposite shifts of the Cd cations and As anions along the  $\langle 110 \rangle$  direction. It can be easily analyzed based on  $4 \times 4 \mathbf{k} \cdot \mathbf{p}$  model Hamiltonian (see Appendix B for details).

Gapping a Dirac point along a high-symmetry line can result in either a Weyl semimetal or topological insulator (TI) [7]. We eliminate the first possibility by employing the monopole mining method [48], which finds no sources or

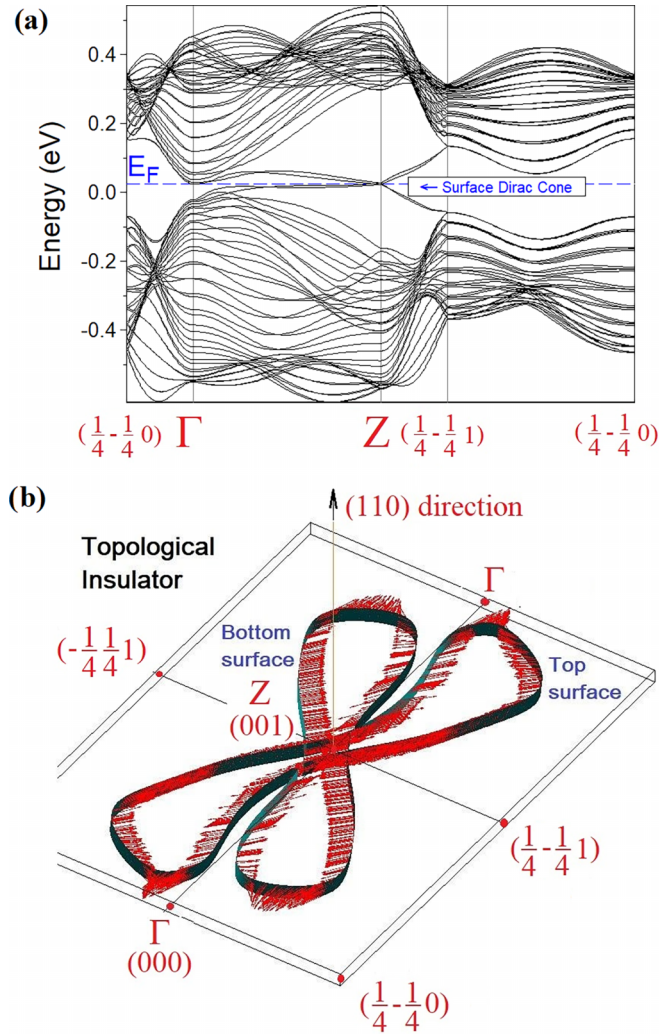


FIG. 5. Forty-layer slab calculation of the tight-binding model fit for the topological insulator phase of  $\text{Cd}_3\text{As}_2$ , showing the (a) band structure and (b) Fermi-arc surface states. Note that the shown region is stretched along the  $k_{(1-10)}$  direction in order to more clearly show the arc shape.

sinks of Berry curvature within the BZ. For the second case, we determine the classification [38,49] of the TI phase by explicitly computing the topological indices on each torus using a discretized plaquette link method [50,51]. This identifies a weak TI phase, which is confirmed by our calculation of the surface energy band states [Fig. 5(a)] with the Dirac cone appearing around the zone boundary Z point of the BZ, and of the Fermi surface sheets crossing the edges of the BZ [Fig. 5(b)] instead of encircling the  $\Gamma$  point as they would for a strong TI.

The Fermi surface of the  $\text{Cd}_3\text{As}_2$  TI phase is qualitatively very similar to the Dirac semimetal phase. It does not resemble typical Dirac cones of topological insulators with circular Fermi surface and helical spin alignments, which are seen in, e.g.,  $\text{Bi}_2\text{Se}_3$ . Here the Fermi surface sheets have long straight regions extended in the  $\Gamma$ -Z direction, as well as the antialigned spin structure at  $(\mathbf{k}, -\mathbf{k})$  opposite  $\mathbf{k}$  points. The only deviations from this are slight spin rotations near the  $\Gamma$  point, where the Dirac node projections were previously

located. This Fermi surface structure would suppress both back- and side-scattering processes, resulting in a highly suppressed scattering for all angles, just as in the Dirac phase. On top of that, since the bulk Dirac points are gapped, no surface-to-bulk scattering is anticipated, at least for the temperatures lower than the gap induced by the structural distortions, and this is another way to interpret low-temperature measurements of the resistivity in  $\text{Cd}_3\text{As}_2$  [18].

## VI. CONCLUSION

In conclusion, based on our accurate numerical fits to the electronic structure of  $\text{Cd}_3\text{As}_2$  Dirac semimetal, its Fermi arcs have been found to be stretching through the edges of the Brillouin zone and producing very long and straight Fermi surfaces. Their particular shape and spin structure results in suppression of both back- and side-scattering effects in the electronic transport, which was explicitly demonstrated by calculating the available phase space to the scattering for the Fermi-arc electrons of the Dirac semimetal phase. A similar suppression mechanism is expected for the surface Dirac cones of a possible topological insulator phase, which can be induced by an inversion-breaking perturbation. Ultra-high carrier mobility and strong resistivity anisotropy at very low temperatures naturally emerges from the present study, which could explain recent resistivity measurements in  $\text{Cd}_3\text{As}_2$ .

Recently, a number of approaches have emerged for engineering topological Dirac states in semiconductor heterostructures [52–54]. The mature fabrication methods developed around these Group III, IV, and V semiconductors enable the creation of heterostructures with precise control over layer thickness, termination, doping, and strain. Since the shape of Fermi-arc surface states is highly dependent on the crystallographic direction of the surface, atomic terminations, surface strain, and material interfaces [55,56], these highly tunable semiconductor heterostructures could be used to engineer long, straight, Fermi-arc states with high mobilities for next-generation electronic devices.

## ACKNOWLEDGMENTS

V.I. is supported by startup funding from Virginia Tech. X.W. was supported by NSFC Grants No. 12188101, No. 11834006, No. 12004170, No. 51721001, and No. 11790311, as well as the excellent program at Nanjing University. X.W. also acknowledges the support from the Tencent Foundation through the Xplorer Prize.

## APPENDIX A: REFINED TWO-ORBITAL TIGHT-BINDING MODEL FOR $\text{Cd}_3\text{As}_2$

For a general  $2 \times 2$  Hamiltonian

$$H_{ab}(\mathbf{k}) = \begin{bmatrix} h_{1\mathbf{k}} & v_{\mathbf{k}} \\ v_{\mathbf{k}}^* & h_{2\mathbf{k}} \end{bmatrix},$$

the eigenvalues are given by

$$\epsilon_{1,2}(\mathbf{k}) = \frac{h_{1\mathbf{k}} + h_{2\mathbf{k}}}{2} \mp \frac{1}{2} \sqrt{(h_{1\mathbf{k}} - h_{2\mathbf{k}})^2 + 4|v_{\mathbf{k}}|^2}.$$

If we start from the LDA band structure of Cd<sub>3</sub>As<sub>2</sub>, we have two dispersive bands, therefore

$$\epsilon_2(\mathbf{k}) - \epsilon_1(\mathbf{k}) = \sqrt{(h_{1\mathbf{k}} - h_{2\mathbf{k}})^2 + 4|v_{\mathbf{k}}|^2}.$$

To determine tight-binding parameters, we use the following lattice translations of the body-centered tetragonal lattice (in units of lattice constants  $a, a, c$  along the  $x, y, z$  axis):

$$A = (1, 0, 0), \quad B = (0, 1, 0), \quad C = (1/2, 1/2, 1/2).$$

$$\begin{aligned} h(k_x, k_y, k_z) &= \sum_R e^{ik_x R_x} e^{ik_y R_y} e^{ik_z R_z} h(R_x, R_y, R_z) \\ &= \epsilon_0 + t_1(e^{ik_x a} + e^{-ik_x a} + e^{ik_y a} + e^{-ik_y a}) + t_2(e^{ik_x a/2} e^{ik_y a/2} e^{ik_z a/2} + \dots) + t_3(e^{ik_z a} + e^{-ik_z a}) \\ &\quad + t_4(e^{ik_x a/2} e^{ik_y a/2} + e^{ik_x a/2} e^{-ik_y a/2} + e^{-ik_x a/2} e^{ik_y a/2} + e^{-ik_x a/2} e^{-ik_y a/2}) + \dots \\ &= \epsilon_0 + 2t_1(\cos k_x a + \cos k_y a) + 8t_2 \cos k_x a/2 \cos k_y a/2 \cos k_z a/2 \\ &\quad + 2t_3 \cos k_z a + 4t_4 \cos k_x a/2 \cos k_y a/2 + \dots \end{aligned}$$

According to the  $\mathbf{k} \cdot \mathbf{p}$  result, we do not anticipate dispersion of  $v_{\mathbf{k}}$  along the 001 line because  $v_{\mathbf{k}} = \lambda(k_x + ik_y)$ . As a result,

$$H_{ab}(0, 0, k_z) = \begin{bmatrix} h_{1\mathbf{k}} & 0 \\ 0 & h_{2\mathbf{k}} \end{bmatrix}$$

and

$$\epsilon_1(0, 0, k_z) = h_1(0, 0, k_z), \quad \epsilon_2(0, 0, k_z) = h_2(0, 0, k_z).$$

Thus, the dispersion along 001 determines  $h(0, 0, k_z)$

Denoting  $t_i = h(R_i)$  we obtain along the 001 direction

$$\begin{aligned} h(0, 0, k_z) &= \sum_R e^{ik_z R_z} h(R_x, R_y, R_z) = \epsilon_0 + 4t_1 + 8t_2 \cos k_z a/2 \\ &\quad + 2t_3 \cos k_z a + 4t_4 + 8t_5 \cos k_z a + 16t_6 \cos k_z a/2 + 8t_7 \cos k_z a + \dots \\ &= \epsilon_0 + 4(t_1 + t_4) + 8(t_2 + 2t_6) \cos k_z a/2 + 2(t_3 + 4t_5 + 4t_7) \cos k_z a + \dots \end{aligned}$$

for the  $\mathbf{k} = (0, 0, 0)2\pi/a$ :

$$h(0, 0, 0) = \epsilon_0 + 4(t_1 + t_4) + 8(t_2 + 2t_6) + 2(t_3 + 4t_5 + 4t_7);$$

for the  $\mathbf{k} = (0, 0, 1)2\pi/a$ :

$$h(0, 0, 1) = \epsilon_0 + 4(t_1 + t_4) - 8(t_2 + 2t_6) + 2(t_3 + 4t_5 + 4t_7);$$

for the  $\mathbf{k} = (0, 0, 1/2)2\pi/a$ :

$$h(0, 0, 1/2) = \epsilon_0 + 4(t_1 + t_4) - 2(t_3 + 4t_5 + 4t_7);$$

for the  $\mathbf{k} = (0, 0, 1/4)2\pi/a$ :

$$h(0, 0, 1/4) = \epsilon_0 + 4(t_1 + t_4) + 8(t_2 + 2t_6)/\sqrt{2};$$

and for the  $\mathbf{k} = (0, 0, 3/4)2\pi/a$ :

$$h(0, 0, 3/4) = \epsilon_0 + 4(t_1 + t_4) - 8(t_2 + 2t_6)/\sqrt{2}.$$

We obtain the following connections between hopping integrals:

$$\epsilon_0 + t_1 + t_4 = [h(0, 0, 0) + h(0, 0, 1) + 2h(0, 0, 1/2)]/16,$$

$$t_2 + 2t_6 = [h(0, 0, 0) - h(0, 0, 1)]/16,$$

$$t_3 + 4t_5 + 4t_7 = [h(0, 0, 0) + h(0, 0, 1) - 2h(0, 0, 1/2)]/8,$$

Nearest-neighbor vectors from the origin are the following:

$$4:R_1 = (\pm 1, 0, 0), (0, \pm 1, 0),$$

$$8:R_2 = (\pm 1/2, \pm 1/2, \pm 1/2),$$

$$2:R_3 = (0, 0, \pm 1),$$

$$4:R_4 = (\pm 1, \pm 1, 0)$$

...

We denote  $\epsilon_0 = h(0)$ ,  $t_i = h(R_i)$ . Generally, for  $h(k_x, k_y, k_z)$  obeying full lattice symmetry, we expect that

$$\epsilon_0 + t_1 + t_4 = [h(0, 0, 1/4) + h(0, 0, 3/4)]/8,$$

$$t_2 + 2t_6 = [h(0, 0, 1/4) - h(0, 0, 3/4)]\sqrt{2}/16,$$

We now interpret the above described two-orbital model as the two LDA energy bands that cross the Fermi level and produce the Dirac point along the  $\Gamma$ -Z line of the BZ. We can interpret these two orbitals in the spinor basis of  $|\uparrow\rangle$  and  $|\downarrow\rangle$  states. We use the LDA extracted values for the first band:

$$\epsilon_1(0, 0, 0) = 0.02 \text{ eV},$$

$$\epsilon_1(0, 0, 1) = -0.41 \text{ eV},$$

$$\epsilon_1(0, 0, 1/2) = -0.09 \text{ eV},$$

$$\epsilon_1(0, 0, 1/4) = -0.01 \text{ eV},$$

$$\epsilon_1(0, 0, 3/4) = -0.24 \text{ eV},$$

which produces

$$\epsilon_0^{(1)}/4 + t_1^{(1)} + t_4^{(1)} = -0.0356 \text{ eV},$$

$$t_2^{(1)} + 2t_6^{(1)} = +0.0269 \text{ eV},$$

$$t_3^{(1)} + 4t_5^{(1)} + 4t_7^{(1)} = -0.0262 \text{ eV}.$$

We need to use  $\epsilon_0^{(1)} > 0$  so that there is gap everywhere in the BZ except the Dirac point. Neglecting the fourth- and higher-order hoppings, this gives us the set of on-site energies and hopping integrals for the first orbital up to third order:

$$\begin{aligned}\epsilon_0^{(1)} &= 0.1 \text{ eV}, & t_1^{(1)} &= -0.0606 \text{ eV}, \\ t_2^{(1)} &= 0.0269 \text{ eV}, & t_3^{(1)} &= -0.0262 \text{ eV}.\end{aligned}$$

Similarly, we use the LDA extracted values for the second band:

$$\begin{aligned}\epsilon_2(0, 0, 0) &= -0.02 \text{ eV}, & \epsilon_2(0, 0, 1) &= 0.55 \text{ eV}, \\ \epsilon_2(0, 0, 1/2) &= 0.35 \text{ eV}, & \epsilon_2(0, 0, 1/4) &= 0.05 \text{ eV}, \\ \epsilon_2(0, 0, 3/4) &= 0.50 \text{ eV},\end{aligned}$$

$$\begin{aligned}\epsilon_0^{(2)}/4 + t_1^{(2)} + t_4^{(2)} &= +0.0769 \text{ eV}, \\ t_2^{(2)} + 2t_6^{(2)} &= -0.0356 \text{ eV}, \\ t_3^{(2)} + 4t_5^{(2)} + 4t_7^{(2)} &= -0.0212 \text{ eV}.\end{aligned}$$

We need to use  $\epsilon_0^{(2)} < 0$  for the fit so that there is a gap everywhere in the BZ except the Dirac point. This gives the second set of on-site energies and hopping integrals for the second orbital up to third order:

$$\begin{aligned}\epsilon_0^{(2)} &= -0.1 \text{ eV}, & t_1^{(2)} &= 0.1019 \text{ eV}, \\ t_2^{(2)} &= -0.0356 \text{ eV}, & t_3^{(2)} &= -0.0212 \text{ eV}.\end{aligned}$$

Finally in  $\mathbf{k} \cdot \mathbf{p}$  theory, the off-diagonal parameter between first (spin up) and second (spin down) orbitals is  $v(\mathbf{k}) = \lambda(k_x + ik_y)$ . The tight-binding representation that leads to this is

$$\begin{aligned}v(\mathbf{k}) &= \sum_{\mathbf{R}} e^{i\mathbf{k}\mathbf{R}} v(\mathbf{R}) = v(100)e^{ik_x} + v(-100)e^{-ik_x} + v(010)e^{ik_y} + v(0-10)e^{-ik_y} \\ &\quad + v(200)e^{ik_x} + v(-200)e^{-ik_x} + v(020)e^{ik_y} + v(0-20)e^{-ik_y} \\ &= \lambda_1(e^{ik_x} - e^{-ik_x})/2i + \lambda_1 i(e^{ik_x} - e^{-ik_x})/2i + \lambda_{11}(e^{ik_x}e^{ik_y} - e^{ik_x}e^{-ik_y} - e^{-ik_x}e^{ik_y} + e^{-ik_x}e^{-ik_y})/(2i)^2 \\ &\quad + \lambda_2(e^{i2k_x} - e^{-i2k_x})/2i + \lambda_2 i(e^{i2k_x} - e^{-i2k_x})/2i \\ &= \lambda_1(\sin k_x + i \sin k_y) + \lambda_2(\sin 2k_x + i \sin 2k_y).\end{aligned}$$

Here we used

$$\begin{aligned}v(+100) &= +\lambda_1/(2i), & v(-100) &= -\lambda_1/(2i), \\ v(0+10) &= +\lambda_1 i/(2i), & v(0-10) &= -\lambda_1 i/(2i), \\ v(+200) &= +\lambda_2/(2i), & v(-200) &= -\lambda_2/(2i), \\ v(0+20) &= +\lambda_2 i/(2i), & v(0-20) &= -\lambda_2 i/(2i).\end{aligned}$$

The best fit is obtained with the use of the parameters

$$\lambda_1 = -0.24 \text{ eV}, \quad \lambda_2 = +0.08 \text{ eV}.$$

The above parameters are used in our tight-binding simulations of the surface states and the transport properties described in the main text.

## APPENDIX B: INVERSION BROKEN DISTORTED STRUCTURE ALONG (110)

Here we want to describe a symmetry-broken phase as caused by a perturbation along the 110 crystallographic line. It could be due to the presence of the contact in an experimental setup or strong electric field applied along (110). Such a perturbation will break the inversion and leave only four symmetry operations of the crystalline group including  $180^\circ$  rotation along (110) as well as reflections within basal and (1-10) planes. Our density functional LDA calculation for such a symmetry-broken phase involves moving the atoms of Cd and As in the opposite direction along (110) to simulate a compatible distortion. The result is plotted on Fig. 6, where one can see a small gap opening in the vicinity of the Dirac point.

We next analyze this result in terms of a generic  $\mathbf{k} \cdot \mathbf{p}$  model. For the Dirac semimetal, such a model has been described many times in the literature (see, e.g., [2]). It consists of two orbitals with  $k$  dispersions  $\pm M(\mathbf{k})$ , where  $M(\mathbf{k}) = M_0 - M_1(k_x^2 + k_y^2) - M_2 k_z^2$ , that interact via the matrix element  $A(k_x \pm ik_y)$ . The parameters  $M_0, M_1, M_2$  should be chosen negative to reproduce band inversion. The model naturally respects all symmetry operations of the tetragonal lattice as is the case of the undistorted tetragonal ( $I4_1/acd$ , No. 142) structure of  $\text{Cd}_3\text{As}_2$ .

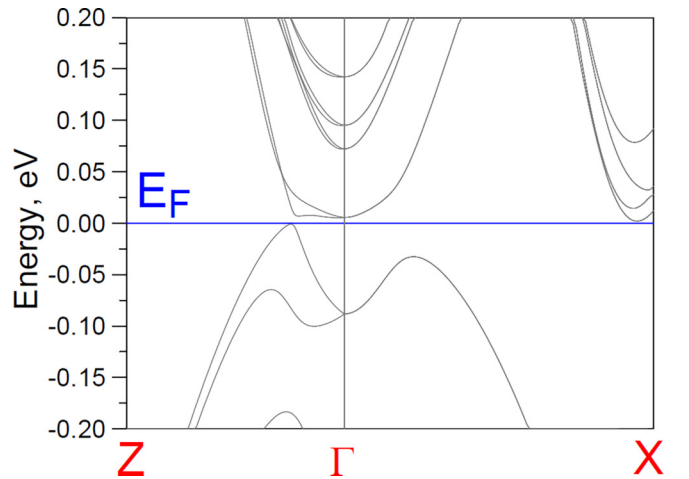


FIG. 6. Electronic structure of the distorted  $\text{Cd}_3\text{As}_2$  that shows a gap opening in the vicinity of Dirac points and results in a weak topological insulator phase.



The lowest-order  $\mathbf{k} \cdot \mathbf{p}$  Hamiltonian that illustrates this scenario reads

$$H(\mathbf{k}) = \begin{bmatrix} +M(\mathbf{k}) & A(k_y + ik_x) & 0 & Bk_z \\ A(k_y - ik_x) & -M(\mathbf{k}) & Ck_z & 0 \\ 0 & Ck_z & +M(\mathbf{k}) & -A(k_y - ik_x) \\ Bk_z & 0 & -A(k_y + ik_x) & -M(\mathbf{k}) \end{bmatrix}.$$

It describes the transition between Dirac semimetal ( $B = C = 0$ ) and topological insulator ( $B, C \neq 0$ ) phases. If we keep off-diagonal parameters  $B$  and  $C$  different, this describes lifting of the degeneracy along  $\Gamma Z$  (001) line of the BZ as seen in our density functional calculation given in Fig. 6.

Next, we convert this  $\mathbf{k} \cdot \mathbf{p}$  Hamiltonian to the refined four orbital tight-binding model. However, the diagonal  $2 \times 2$  subblocks of this Hamiltonian translate to the two-orbital tight-binding model that we already discussed for the Dirac semimetal phase. The off-diagonal terms (the ones with the coefficients  $C$  and  $D$ ) are periodized with the substitution of  $k_z \rightarrow \sin k_z c$ . The numbers  $C$  and  $D$  are small and describe the perturbation that gap the Dirac points and result in the weak topological insulator state of  $\text{Cd}_3\text{As}_2$ . We use its actual values  $C = D = 0.0068$  eV for the plots presented in the main text.

- 
- [1] M. v. Stackelberg and R. Paulu, Untersuchungen an den phosphiden und arseniden des zinks und cadmiums. Das  $\text{Zn}_3\text{P}_2$ -Gitter, *Z. Phys. Chem.* **28B**, 427 (1935).
- [2] Z. Wang, H. Weng, Q. Wu, X. Dai, and Z. Fang, Three-dimensional Dirac semimetal and quantum transport in  $\text{Cd}_3\text{As}_2$ , *Phys. Rev. B* **88**, 125427 (2013).
- [3] S. Borisenko, Q. Gibson, D. Evtushinsky, V. Zabolotnyy, B. Buechner, and R. J. Cava, Experimental realization of a three-dimensional Dirac semimetal, *Phys. Rev. Lett.* **113**, 027603 (2014).
- [4] M. Neupane, S.-Y. Xu, R. Sankar, A. Raman, B. Nasser, L. Guang, C. Liu, I. Belopolski, T.-R. Chang, H.-T. Jeng *et al.*, Observation of a three-dimensional topological Dirac semimetal phase in high-mobility  $\text{Cd}_3\text{As}_2$ , *Nat. Commun.* **5**, 3786 (2014).
- [5] H. Yi, Z. Wang, C. Chen, Y. Shi, Y. Feng, A. Liang, Z. Xie, S. He, J. He, Y. Peng *et al.*, Evidence of topological surface state in three-dimensional Dirac semimetal  $\text{Cd}_3\text{As}_2$ , *Sci. Rep.* **4**, 6106 (2014).
- [6] S. Roth, H. Lee, A. Sterzi, M. Zacchigna, A. Politano, R. Sankar, F. C. Chou, G. Di Santo, L. Petaccia, O. V. Yazyev, and A. Crepaldi, Reinvestigating the surface and bulk electronic properties of  $\text{Cd}_3\text{As}_2$ , *Phys. Rev. B* **97**, 165439 (2018).
- [7] B. Yan and C. Felser, Topological materials: Weyl semimetals, *Annu. Rev. Condens. Matter Phys.* **8**, 337 (2017).
- [8] Z. Gao, M. Hua, H. Zhang, and X. Zhang, Classification of stable Dirac and Weyl semimetals with reflection and rotational symmetry, *Phys. Rev. B* **93**, 205109 (2016).
- [9] D. Neubauer, J. P. Carbotte, A. A. Nateprov, A. Loehle, M. Dressel, and A. V. Pronin, Interband optical conductivity of the [001]-oriented Dirac semimetal  $\text{Cd}_3\text{As}_2$ , *Phys. Rev. B* **93**, 121202(R) (2016).
- [10] G. S. Jenkins, C. Lane, B. Barbiellini, A. B. Sushkov, R. L. Carey, F. Liu, J. W. Krizan, S. K. Kushwaha, Q. Gibson, T.-R. Chang *et al.*, Three-dimensional Dirac cone carrier dynamics in  $\text{Na}_3\text{Bi}$  and  $\text{Cd}_3\text{As}_2$ , *Phys. Rev. B* **94**, 085121 (2016).
- [11] G. Chang, J.-X. Yin, T. Neupert, D. S. Sanchez, I. Belopolski, S. S. Zhang, T. A. Cochran, Z. Cheng, M. C. Hsu, S.-M. Huang *et al.*, Unconventional photocurrents from surface Fermi arcs in topological chiral semimetals, *Phys. Rev. Lett.* **124**, 166404 (2020).
- [12] G. Zheng, M. Wu, H. Zhang, W. Chu, W. Gao, J. Lu, Y. Han, J. Yang, H. Du, W. Ning *et al.*, Recognition of Fermi-arc states through the magnetoresistance quantum oscillations in Dirac semimetal  $\text{Cd}_3\text{As}_2$  nanoplates, *Phys. Rev. B* **96**, 121407(R) (2017).
- [13] Y. Miyazaki, Y. Yu, T. Yokouchi, K. Shibata, Y. Chen, H. Arisawa, T. Mizoguchi, E. Saitoh, and Y. Shiomi, Quantum oscillations from Fermi arc surface states in  $\text{Cd}_3\text{As}_2$  submicron wires, *Phys. Rev. Res.* **4**, L022002 (2022).
- [14] C. Zhang, A. Narayan, S. Lu, Z. Shiheng, Z. Jinglei, H. Zhang, Z. Ni, X. Yuan, Y. Liu, J.-H. Park *et al.*, Evolution of Weyl orbit and quantum Hall effect in Dirac semimetal  $\text{Cd}_3\text{As}_2$ , *Nat. Commun.* **8**, 1272 (2017).
- [15] P. J. W. Moll, N. L. Nair, T. Helm, A. Potter, I. Kimchi, A. Vishwanath, and J. G. Analytis, Transport evidence for Fermi-arc-mediated chirality transfer in the Dirac semimetal  $\text{Cd}_3\text{As}_2$ , *Nature (London)* **535**, 266 (2016).
- [16] O. F. Shoron, T. Schumann, M. Goyal, D. A. Kealhofer, and S. Stemmer, Field-effect transistors with the three-dimensional Dirac semimetal cadmium arsenide, *Appl. Phys. Lett.* **115**, 062101 (2019).
- [17] Y. Zhao, H. Liu, C. Zhang, H. Wang, J. Wang, Z. Lin, Y. Xing, L. Ying, H. Lu, J. Liu *et al.*, Anisotropic Fermi surface and quantum limit transport in high mobility three-dimensional Dirac semimetal  $\text{Cd}_3\text{As}_2$ , *Phys. Rev. X* **5**, 031037 (2015).
- [18] T. Liang, Q. Gibson, A. Quinn, N. Mazhar, M. Liu, R. J. Cava, and N. P. Ong, Ultrahigh mobility and giant magnetoresistance in the Dirac semimetal  $\text{Cd}_3\text{As}_2$ , *Nat. Mater.* **14**, 280 (2015).
- [19] B. C. Lin, S. Wang, A.-Q. Wang, Y. Li, R.-R. Li, K. Xia, D. Yu, and Z.-M. Liao, Electric control of Fermi arc spin transport in individual topological semimetal nanowires, *Phys. Rev. Lett.* **124**, 116802 (2020).
- [20] S. Tang, W. Chen, Q. Ye, Z. Liu, Q. Wu, Y. Du, X. Zhou, and X. Xiao, Electron transport probing the electrically tunable topological phase transition in a Dirac semimetal, *Phys. Rev. B* **104**, 205427 (2021).
- [21] Y. Baba, F. Domínguez-Adame, G. Platero, and R. A. Molina, Rashba coupling and spin switching through surface states of Dirac semimetals, *New J. Phys.* **23**, 023008 (2021).
- [22] S. Kobayashi and M. Sato, Topological superconductivity in Dirac semimetals, *Phys. Rev. Lett.* **115**, 187001 (2015).
- [23] H. Wang, H. Wang, H. Liu, H. Lu, W. Yang, S. Jia, X.-J. Liu, X. C. Xie, J. Wei, and J. Wang, Observation of superconductivity induced by a point contact on 3D Dirac semimetal  $\text{Cd}_3\text{As}_2$  crystals, *Nat. Mater.* **15**, 38 (2016).

- [24] O. O. Shvetsov, V. D. Esin, A. V. Timonina, N. N. Kolesnikov, and E. V. Deviatov, Surface superconductivity in a three-dimensional  $\text{Cd}_3\text{As}_2$  semimetal at the interface with a gold contact, *Phys. Rev. B* **99**, 125305 (2019).
- [25] C. Huang, B. Zhou, H. Zhang, B. Yang, R. Liu, H. Wang, Y. Wan, K. Huang, Z. Liao, E. Zhang *et al.*, Proximity-induced surface superconductivity in Dirac semimetal  $\text{Cd}_3\text{As}_2$ , *Nat. Commun.* **10**, 2217 (2019).
- [26] C.-Z. Li, C. Li, L.-X. Wang, S. Wang, Z.-M. Liao, A. Brinkman, and D.-P. Yu, Bulk and surface states carried supercurrent in ballistic Nb-Dirac semimetal  $\text{Cd}_3\text{As}_2$  nanowire-Nb junctions, *Phys. Rev. B* **97**, 115446 (2018).
- [27] H. Pan, M. Wu, Y. Liu, Y. Ying, and A. Shengyuan, Electric control of topological phase transitions in Dirac semimetal thin films, *Sci. Rep.* **5**, 14639 (2015).
- [28] A. Mosca Conte, O. Pulci, and F. Bechstedt, Electronic and optical properties of topological semimetal  $\text{Cd}_3\text{As}_2$ , *Sci. Rep.* **7**, 45500 (2017).
- [29] S. Baidya and D. Vanderbilt, First-principles theory of the Dirac semimetal  $\text{Cd}_3\text{As}_2$  under Zeeman magnetic field, *Phys. Rev. B* **102**, 165115 (2020).
- [30] A. Rancati, N. Pournaghavi, M. F. Islam, A. Debernardi, and A. C. M. Canali, Impurity-induced topological phase transitions in  $\text{Cd}_3\text{As}_2$  Dirac semimetals, *Phys. Rev. B* **102**, 195110 (2020).
- [31] M. N. Ali, Q. Gibson, S. Jeon, B. B. Zhou, A. Yazdani, and R. J. Cava, The crystal and electronic structures of  $\text{Cd}_3\text{As}_2$ , the three-dimensional electronic analogue of graphene, *Inorg. Chem.* **53**, 4062 (2014).
- [32] X. Wan, A. M. Turner, A. Vishwanath, and S. Y. Savrasov, Topological semimetal and Fermi-arc surface states in the electronic structure of pyrochlore iridates, *Phys. Rev. B* **83**, 205101 (2011).
- [33] G. Resta, S.-T. Pi, X. Wan, and S. Y. Savrasov, High surface conductivity of Fermi-arc electrons in Weyl semimetals, *Phys. Rev. B* **97**, 085142 (2018).
- [34] Y. Nakazawa, M. Uchida, S. Nishihaya, M. Kriener, Y. Kozuka, Y. Taguchi, and M. Kawasaki, Structural characterisation of high-mobility  $\text{Cd}_3\text{As}_2$  films crystallised on  $\text{SrTiO}_3$ , *Sci. Rep.* **8**, 2244 (2018).
- [35] B. M. Wang, Y. Zhu, H. C. Travaglini, R. Sun, S. Y. Savrasov, W. Hahn, K. van Benthem, and D. Yu, Spatially dispersive helicity-dependent photocurrent in Dirac semimetal  $\text{Cd}_3\text{As}_2$  nanobelts, *Phys. Rev. B* **108**, 165405 (2023).
- [36] A. Pietraszko and K. Lukaszewicz, A refinement of the crystal structure of  $\alpha$ - $\text{Cd}_3\text{As}_2$ , *Acta Crystallogr. B* **25**, 988 (1969).
- [37] G. A. Steigmann and J. Goodyear, The crystal structure of  $\text{Cd}_3\text{As}_2$ , *Acta Crystallogr. B* **24**, 1062 (1968).
- [38] L. Fu, C. L. Kane, and E. J. Mele, Topological insulators in three dimensions, *Phys. Rev. Lett.* **98**, 106803 (2007).
- [39] M. Kargarian, M. Randeria, and Y.-M. Lu, Are the surface Fermi arcs in Dirac semimetals topologically protected? *Proc. Natl. Acad. Sci. USA* **113**, 8648 (2016).
- [40] C. Le, X. Wu, S. Qin, Y. Li, R. Thomale, F.-C. Zhang, and J. Hu, Dirac semimetal in  $\text{CuI}$  without surface Fermi arcs, *Proc. Natl. Acad. Sci. USA* **115**, 8311 (2018).
- [41] S. Y. Savrasov, Linear-response theory and lattice dynamics: A muffin-tin-orbital approach, *Phys. Rev. B* **54**, 16470 (1996).
- [42] S. H. Vosko, L. Wilk, and M. Nusair, Accurate spin-dependent electron liquid correlation energies for local spin density calculations: A critical analysis, *Can. J. Phys.* **58**, 1200 (1980).
- [43] M. Z. Hasan and C. L. Kane, Colloquium: Topological insulators, *Rev. Mod. Phys.* **82**, 3045 (2010).
- [44] N. P. Armitage, E. J. Mele, and A. Vishwanath, Weyl and Dirac semimetals in three-dimensional solids, *Rev. Mod. Phys.* **90**, 015001 (2018).
- [45] P. B. Allen, New method for solving Boltzmann's equation for electrons in metals, *Phys. Rev. B* **17**, 3725 (1978).
- [46] S. Y. Savrasov, D. Y. Savrasov, and O. K. Andersen, Linear-response calculations of electron-phonon interactions, *Phys. Rev. Lett.* **72**, 372 (1994).
- [47] C. Zhang, Z. Ni, J. Zhang, X. Yuan, Y. Liu, Y. Zou, Z. Liao, Y. Du, A. Narayan, H. Zhang *et al.*, Ultrahigh conductivity in Weyl semimetal NbAs nanobelts, *Nat. Mater.* **18**, 482 (2019).
- [48] V. Ivanov and S. Y. Savrasov, Monopole mining method for high-throughput screening for Weyl semimetals, *Phys. Rev. B* **99**, 125124 (2019).
- [49] L. Fu and C. L. Kane, Topological insulators with inversion symmetry, *Phys. Rev. B* **76**, 045302 (2007).
- [50] T. Fukui and Y. Hatsugai, Quantum spin Hall effect in three dimensional materials: Lattice computation of  $Z_2$  topological invariants and its application to Bi and Sb, *J. Phys. Soc. Jpn.* **76**, 053702 (2007).
- [51] W. Feng, J. Wen, J. Zhou, D. Xiao, and Y. Yao, First-principles calculation of  $Z_2$  topological invariants within the FP-LAPW formalism, *Comput. Phys. Commun.* **183**, 1849 (2012).
- [52] D. Zhang, W. Lou, M. Miao, S.-C. Zhang, and K. Chang, Interface-induced topological insulator transition in GaAs/Ge/GaAs quantum wells, *Phys. Rev. Lett.* **111**, 156402 (2013).
- [53] M. Patrashin, N. Sekine, K. Akahane, A. Kasamatsu, and I. Hosako, Dirac semimetal states in engineered zero-gap InAs/GaInSb superlattices, *Physica Status Solidi (b)* **256**, 1800726 (2019).
- [54] C.-Z. Xu, Y.-H. Chan, Y. Chen, P. Chen, X. Wang, C. Dejoie, M.-H. Wong, J. A. Hlevyack, H. Ryu, H.-Y. Kee *et al.*, Elemental topological Dirac semimetal:  $\alpha$ -Sn on InSb(111), *Phys. Rev. Lett.* **118**, 146402 (2017).
- [55] Q. Xu, E. Liu, W. Shi, L. Muechler, J. Gayles, C. Felser, and Y. Sun, Topological surface Fermi arcs in the magnetic Weyl semimetal  $\text{Co}_3\text{Sn}_2\text{S}_2$ , *Phys. Rev. B* **97**, 235416 (2018).
- [56] A. Rossi, V. Ivanov, S. Sreedhar, A. L. Gross, Z. Shen, E. Rotenberg, A. Bostwick, C. Jozwiak, V. Taufour, S. Y. Savrasov, and I. M. Vishik, Electronic structure and topology across  $T_c$  in the magnetic Weyl semimetal  $\text{Co}_3\text{Sn}_2\text{S}_2$ , *Phys. Rev. B* **104**, 155115 (2021).